

# Depth-varying seismogenesis on an oceanic detachment fault at 13°20'N on the Mid-Atlantic Ridge

Timothy J. Craig<sup>1,\*</sup>, Ross Parnell-Turner<sup>2</sup>

<sup>1</sup> Institute of Geophysics and Tectonics,  
School of Earth and Environment, University of Leeds,  
Leeds, LS2 9JT, UK.

<sup>2</sup> Department of Geology and Geophysics,  
Woods Hole Oceanographic Institution,  
Woods Hole Road, Woods Hole, MA 02543, USA.

\*Corresponding author: t.j.craig[at]leeds.ac.uk

August 31, 2017

## Abstract

Extension at slow- and intermediate-spreading mid-ocean ridges is commonly accommodated through slip on long-lived faults called oceanic detachments. These curved, convex-upward faults consist of a steeply-dipping section thought to be rooted in the lower crust or upper mantle which rotates to progressively shallower dip-angles at shallower depths. The commonly-observed result is a domed, sub-horizontal oceanic core complex at the seabed. Although it is accepted that detachment faults can accumulate kilometre-scale offsets over millions of years, the mechanism of slip, and their capacity to sustain the shear stresses necessary to produce large earthquakes, remains debated. Here we present a comprehensive seismological study of an active oceanic detachment fault system on the Mid-Atlantic Ridge near 13°20'N, combining the results from a local ocean-bottom seismograph deployment with waveform inversion of a series of larger teleseismically-observed earthquakes. The unique coincidence of these two datasets provides a comprehensive definition of rupture on the fault, from the uppermost mantle to the seabed. Our

results demonstrate that although slip on the deep, steeply-dipping portion of detachment faults is accommodated by failure in numerous microearthquakes, the shallow, gently-dipping section of the fault within the upper few kilometres is relatively strong, and is capable of producing large-magnitude earthquakes. This result brings into question the current paradigm that the shallow sections of oceanic detachment faults are dominated by low-friction mineralogies and therefore slip aseismically, but is consistent with observations from continental detachment faults. Slip on the shallow portion of active detachment faults at relatively low angles may therefore account for many more large-magnitude earthquakes at mid-ocean ridges than previously thought, and suggests that the lithospheric strength at slow-spreading mid-ocean ridges may be concentrated at shallow depths.

## 1 Introduction

Earthquake activity at mid-ocean ridges provides an insight into the thermal and rheological state of the lithosphere as it is created and subsequently deformed (e.g. Sykes, 1967). At slow-spreading ridges, a significant portion of plate separation may be accommodated by slip on long-lived detachment faults, which are thought to initiate at steep dips and then roll over to become sub-horizontal at the seafloor (Cann et al., 1997; Morris et al., 2009). This process leads to the exhumation of lower crustal and upper mantle rocks at the seabed, which often form kilometre-scale domes called oceanic core complexes (OCCs; Tucholke et al., 1998; MacLeod et al., 2002; Dick et al., 2008; Escartin and Canales, 2011).

While seafloor mapping and sampling, and active-source seismic imaging provide a static picture of these features (e.g. Dick, 1989; Cann et al., 1997; Blackman et al., 2009), the subsurface mechanics of the process of roll-over remains enigmatic. Short-duration local ocean bottom seismograph (OBS) experiments have shown that microearthquakes in these settings consistently occur at depths between 3 and 7 km below seafloor (bsf; Toomey et al., 1985; Kong et al., 1992; Wolfe et al., 1995; Grevemeyer et al., 2013). Some of these earlier studies lacked the high-resolution bathymetry necessary to identify detachment faults prior to deployment, and hence used networks

not optimised for studying earthquakes associated with these faults. Two deployments of densely-spaced OBS networks specifically targeting identified active core complexes in the North Atlantic Ocean have shown that the pattern of microearthquakes defines a steep-dipping planar normal fault surface at depth. However rupture at depths shallower than 4 km bsf remains undetected (deMartin et al., 2007; Parnell-Turner et al., 2017). This apparent lack of shallow seismicity has been suggested to be the result of fractured, permeable crust being incapable of supporting sufficient stresses to produce earthquakes, or the presence of hydrothermally-altered fault gouge material leading to aseismic slip (deMartin et al., 2007; Grevemeyer et al., 2013). In contrast, continental detachment faults associated with metamorphic core complexes, for example in Papua New Guinea, may be capable of hosting large-magnitude, shallowly-dipping normal faulting earthquakes on their uppermost sections (Abers, 1991; Abers et al., 1997), although recent geodetic work instead suggests much of the slip may be accommodated aseismically (Wallace et al., 2014).

A large proportion of the slow-spreading Mid-Atlantic Ridge (MAR) shows evidence for detachment faulting and the accretion of oceanic crust through OCC formation (Smith et al., 2006; Escartín et al., 2008). Studies of teleseismically-detected earthquakes at slow-spreading ridges have shown that events in the median valley have typical focal depths of 1–4 km bsf, and dip angles of  $\sim 45^\circ$  (Huang et al., 1986), consistent with global surveys of large earthquakes at other slow-spreading ridges (Jemsek et al., 1986; Solomon and Huang, 1987). Lacking the constraints necessary to relate these earthquakes to a particular fault, they have been assumed to be related to planar rift-border faults, and not to be associated with detachment faulting. This assumption, however, contrasts with evidence that detachment-dominated segments of the Mid-Atlantic Ridge generate more earthquakes in both teleseismic and hydroacoustic catalogues (Escartín et al., 2008; Olive and Escartín, 2016), suggesting a link between the presence of detachment faulting and the production of large mid-ocean ridge earthquakes.

Hence, three apparently disparate modes of detachment fault behavior have been identified seismologically. First, dominantly aseismic, uncoupled

behaviour is expected for oceanic detachments associated with weak, low friction mineralogies; second, high-moment-release, teleseismically-detected earthquakes are observed along sections of detachment-fault dominated mid-ocean ridge segments; and third, large-magnitude earthquakes are associated with detachment faulting bounding metamorphic core complexes on the continents. In an attempt to characterise the full seismogenic behaviour of a detachment fault across the complete range of observational scales, we consider the seismicity associated with an actively slipping oceanic detachment fault on the MAR near  $13^{\circ}20'N$ , integrating the results from a local OBS deployment with observations of co-located large earthquakes from the global seismic network.

## 2 Seismicity near the $13^{\circ}20'N$ detachment

We focus on the area near  $13^{\circ}20'N$  on the MAR, where an active OCC has been previously extensively surveyed and sampled (Smith et al., 2006; MacLeod et al., 2009; Mallows and Searle, 2012; Escartín et al., 2017; Bonnemains et al., 2017). The exposed fault surface has prominent spreading-parallel corrugations, and is thought to record  $\sim 9$  km of heave since its initiation at  $\sim 0.4$  Ma (MacLeod et al., 2009; Mallows and Searle, 2012).

In 2014, an array of 25 OBSs detected  $\sim 240,000$  microearthquakes near the  $13^{\circ}20'N$  detachment fault over a period of six months (Parnell-Turner et al., 2017). There are two domains of seismicity: reverse-faulting earthquakes beneath the dome at 3–7 km bsf, attributed to internal compression within the bending footwall; and normal-faulting earthquakes towards the centre of the axial valley, at depths of 5–12 km bsf (Figure 1 and histograms on Figures 4a and 5). The along-axis pattern of normal-faulting microearthquakes suggests that at depth, the active detachment fault extends beyond the limits of the exposed corrugated surface. These normal faulting earthquakes have a composite focal mechanism indicating slip on a steeply eastward-dipping plane (see Supplementary Table 1), interpreted to be the downdip portion of the detachment fault in the region where a coherent fault zone forms. The depth extent and apparent dip of normal-faulting mi-



117 croearthquakes is consistent with that observed at the active Trans-Atlantic  
 118 Geotraverse (TAG) detachment near 26°N on the MAR (deMartin et al.,  
 119 2007). The lack of shallow microearthquakes at these two locations means  
 120 that the style of deformation (e.g., aseismic slip, or seismic failure in large  
 121 or small earthquakes) on the shallow, roll-over portion of detachment faults  
 122 remains uncertain.

123 Over the last decade, three large-magnitude, teleseismically-detected normal-  
 124 faulting earthquakes have occurred in the vicinity of the 13°20'N OCC. A  
 125  $M_w$  5.7 event that occurred on the 7<sup>th</sup> December 2008 (hereafter referred to  
 126 as the 2008 mainshock) was followed a day later by a  $M_w$  5.5 aftershock, and  
 127 a third event,  $M_w$  5.7, occurred on 20<sup>th</sup> October 2016. The ability to relate a  
 128 given earthquake with a specific fault near the mid-ocean ridge is hampered  
 129 by the uncertainty in earthquake location and the absence of near-field data.  
 130 In order to overcome this limitation, we seek to determine the most likely  
 131 hypocentral location for these three events, and therefore their relationship  
 132 to the local tectonic structures, by evaluating five possible scenarios. First,  
 133 that slip occurred on the shallow portion of the 13°20'N detachment which  
 134 lacks microearthquakes; second, that these events are co-located with mi-  
 135 croearthquakes on the steeper, deeper detachment surface; third, that these  
 136 events are shallow antithetic events within the 13°20'N detachment footwall  
 137 block; fourth, that they represent breakup of the detachment hanging wall in  
 138 the formation of rider blocks; or fifth, that they are unrelated to the 13°20'N  
 139 detachment fault and occurred on another fault nearby.

### 140 **3 Constraints on earthquake location**

141 Earthquake locations based on globally-observed travel times for these earth-  
 142 quakes indicate that they all occurred within 10 km of the active 13°20'N  
 143 detachment (Figure 1, Table S2; International Seismological Centre 2014). In  
 144 particular, the 2016 event co-locates with the 13°20'N detachment, slightly  
 145 up-dip of the observed microseismicity. Quoted catalogue uncertainties sug-  
 146 gest that these locations are accurate to  $\sim \pm 10$  km [National Earthquake  
 147 Information Center; NEIC], comparable to the mean error in global seis-

148 mological hypocentre locations, based on geodetic calibration (Lohman and  
149 Simons, 2005; Weston et al., 2012). Independently calculated locations for  
150 these earthquakes from different agencies show a strong clustering within  
151 this level of uncertainty (see Figure 1 and Table S1). Although absolute  
152 locations for these earthquakes are limited by the lack of any near-source  
153 data, improved data coverage between 2008 and 2016 suggests that the 2016  
154 location is probably more reliable. Despite these improvements, attributing  
155 these events to specific tectonic structures, and relating them to one another,  
156 remains difficult.

157 We relocate the three teleseismically-observed earthquakes relative to one  
158 another using inter-event times determined using waveform cross-correlation  
159 (see Figure 3). This approach refines inter-event distances, although it  
160 does not provide absolute locations relative to geographic features (such as  
161 the 13°20'N OCC). Exploiting the broad-scale similarity in mechanism and  
162 source duration between the three teleseismically-observed earthquakes (see  
163 Section 4), we relocate them relative to each other on the basis of relative  
164 travel times derived from cross-correlation of the  $P$  and  $S$  waves. We use  
165 a correlation window of 45 s, starting 5 s before the predicted phase arrival  
166 time. Relative travel times are computed using all three components (vertical  
167 for the  $P$  wave, east and north for the  $S$  wave). We initially use all stations  
168 that cover the observation periods for at least two of the three events con-  
169 sidered, and then limit the dataset based on the ability to visually identify  
170 arrivals in the waveforms, and on the magnitude of the computed cross cor-  
171 relation coefficient, using a threshold value of 0.5. Figure S1 shows the full  
172 station set used for  $P$  and  $S$  waves, overlain on the radiation pattern for the  
173 2016 earthquake (those for 2008 are similar). Note that station coverage is  
174 not the same for all three earthquakes, leading to varying sets of station pairs  
175 for the three event-pairs possible. Whilst the majority of stations active in  
176 2008 cover both of the earthquakes in this year, the smaller magnitude of  
177 the 8<sup>th</sup> December 2008 event leads to a smaller number of stations with clear  
178 arrivals for both events.

179 We use a tapered frequency band, optimised between 0.05 and 1 Hz, for  
180 the cross correlation. Expanding this band to incorporate higher frequencies

181 initially leads to a similar location offset, but the inter-event coherence, par-  
182 ticularly to the 2008 aftershock, decays rapidly above 1 Hz (demonstrated in  
183 Figure 3), leading to a decrease in the number of reliable inter-event travel  
184 times. For the final set of relocations presented in Figure 2, we use 309 *P*-  
185 wave event-pairs, and 269 *S*-wave pairs, with average cross-correlation coeffi-  
186 cients of 0.75 and 0.85, respectively. Prior to relocation, the mean inter-event  
187 travel-time residual is 1.02 s. After relocation, the residual decreases to 0.34  
188 s (residual populations are shown on Figure 2b,c).

189 We test the relocation results by limiting the dataset to those those sta-  
190 tions at epicentral distances of  $<30^\circ$  (32 *P*-wave and 22 *S*-wave pairs) which  
191 should be more sensitive to lateral offsets in location. This refinement leads  
192 to a similar set of relocations, where the 2008 mainshock and the 2016 event  
193 occur within one rupture length of each other ( $\sim 6$  km; see below). The 2008  
194 aftershock is offset to the north and west, although there is some difference  
195 in the magnitude of the shift for this event (Figure 2). Similarly, reloca-  
196 tions using datasets limited to *P*-wave and *S*-wave arrivals alone (Figure 2a)  
197 produces the same overall pattern across the three earthquakes, with the  
198 main variation in the distance, but not direction, of the offset to the 2008  
199 aftershock.

200 Although hampered by scant near-source data (nearest stations  $>14^\circ$  epi-  
201 central distance), the relocations conclusively indicate that the 2008 main-  
202 shock and 2016 event (earthquakes of similar magnitude) occurred near to  
203 one another. Plate spreading rates in this area are unlikely to be sufficient  
204 to accumulate enough strain to produce a  $M_w$  5.7 earthquake in the 8-year  
205 inter-event period, leading us to suggest that these two earthquakes likely  
206 occurred on adjoining segments of the same fault, rather than repeated rup-  
207 ture of the same fault patch. The causative feature must therefore be large  
208 enough to sustain a combined moment release equal to a single  $M_w$  5.9 event.

209 In contrast to the absolute catalogue locations, the smaller 2008 after-  
210 shock appears to locate to the northwest, rather than northeast, of the other  
211 two events considered, although the degree of the westward shift is poorly  
212 constrained (see Figure 2).

213 A northwards offset for the 2008 aftershock is common to both the relative

214 and absolute relocations, whereas the direction of the east-west offset changes  
 215 using the two different techniques. Precise onset times of the direct *P*-wave  
 216 are difficult to determine from the waveforms visually, particularly for the  
 217 lower-amplitude *P*-wave arrivals from the smaller 2008 mainshock, where the  
 218 onset amplitude is often within the level of the background noise. As a result,  
 219 the absolute location for this smaller event is less well constrained than for  
 220 the larger, and hence better resolved earthquakes. We therefore rely on the  
 221 absolute locations for the 2008 mainshock and 2016 event, and suggest that  
 222 the 2008 aftershock is somewhere to the north, although its precise location  
 223 is poorly determined. Any potential causative relationship between the two  
 224 earthquakes in 2008 is unknown, but if the mechanism relating these two  
 225 events is assumed to be static stress transfer, then the east-west offset of  
 226 the aftershock relative to the 2008 mainshock is likely to be less than the  
 227 northwards offset.

228 In the frequency band used for relocation, similarity in overall mechanism  
 229 and locations of the three earthquakes allow their relative times to be deter-  
 230 mined. At higher frequencies ( $> 1$  Hz), similarity between the waveforms for  
 231 the two larger events remains apparent, indicating their proximity to one an-  
 232 other and similar influence of near-source effects on the waveform. Waveforms  
 233 for the 2008 aftershock, while similar to the other events at low frequencies,  
 234 are notably different at higher frequencies, indicating a marginally different  
 235 rupture process and near-source scattering effects (Figure 3).

## 236 4 Source mechanisms and fault geometry

237 To supplement the relative and absolute constraints on the earthquake loca-  
 238 tions, we use teleseismic waveform inversion to constrain the source mecha-  
 239 nism, rupture duration and depth for these three earthquakes using *P*- and  
 240 *SH*-waves, treating each earthquake as a finite-duration point-source cen-  
 241 troid.

242 We invert long-period waveforms observed at teleseismic distances ( $30^\circ$ –  
 243  $80^\circ$  epicentral distance) to determine earthquake mechanism parameters, cen-  
 244 troid depth, moment, and source duration, using the approach of Zwick et al.

(1994). Our method follows that previously used for mid-ocean ridge earthquakes (Huang et al., 1986; Jemsek et al., 1986; Huang and Solomon, 1987), and for the determination of earthquake source parameters in other oceanic settings (Abers, 1991; Abers et al., 1997; Tilmann et al., 2010; Craig et al., 2014). The best-fit parameters for each earthquake are detailed in Table S1. Observed waveforms and best-fit synthetics are shown in Figures S2–S4.

Fifty seismograms with the best azimuthal distribution were selected, using data available from the Incorporated Research Institutions for Seismology Data Management Center (IRIS DMC). We invert a section of the waveform starting from the initial onset of the direct arrival (manually picked from broadband data), and encompassing the direct arrival ( $P$ ,  $S$ ) and principal depth phases ( $pP$ ,  $sP$ ,  $sS$ ). The inversion window for  $P$ -waves was limited to exclude subsequent water multiples, and for  $S$ -waves was limited to exclude any predicted interaction with  $SKS$  arrivals. Waveforms were weighted in the inversion based on azimuthal density, and  $S$ -waveforms were manually weighted down by a factor of 0.5 to compensate for their increased amplitude relative to the  $P$ -wave.

Each earthquake source was parametrised as a finite-duration rupture of a point source, constrained to be a double-couple. The source duration was parametrised as four 1-second elements with independent amplitudes. No improvement in waveform fit was achieved when a longer duration source was tested, and in many cases the final element of the allowed source time function has near-zero amplitude. Hence, for each earthquake we invert for nine parameters: strike, dip, rake, centroid depth, moment, and a four-element source time function.

We use a near-source velocity structure based on the local model derived from a seismic refraction experiment carried out in 2016 in the 13°N area, averaged into a simple half-space (Simão et al., 2016). A water layer is added over the solid Earth structure, with initial thickness from local bathymetry shown in Figure 1. Small adjustments to the water layer thickness are then made to best match the mean periodicity of observed  $P$ -wave water multiples. In common with previous work at mid-ocean ridges we find that the inclusion of a Moho, and the transition to faster mantle velocities below it, improves

the waveform fit for solutions with sub-Moho depths (Huang et al., 1986; Jemsek et al., 1986; Huang and Solomon, 1987). This approach, however, fails to produce solutions that fit better than those located above the Moho, i.e. within the crust, and we hence present results using the simple half-space model. Routine values of 1 and 4 s (for  $P$ - and  $SH$ -waves, respectively) are used for the attenuation parameter  $t^*$  (Futterman, 1962).

Best-fit solutions are plotted in Figure 1a, and detailed in Table 1 and Figures S2–S4. Sensitivity tests for depth and dip were performed by fixing the given parameters, and inverting for the best-fit solution. When testing for depth sensitivity, only centroid depth is fixed while all other parameters are free to vary. When testing for dip sensitivity, dip is fixed, centroid depth is fixed at the overall best-fit value, while all other parameters are free to vary. For sensitivity to dip, two minima occur due to the inherent inability to distinguish between the actual fault plane and the conjugate auxiliary plane in the focal mechanism (Figures 4, 5, and 6).

Centroid depths of all three earthquakes are determined to be within the upper oceanic lithosphere, at depths of  $< 5$  km bsf (Figures 4, 5, 6, and Figures S2–S4). Forcing the source depth to be  $> 5$  km leads to progressively worse fits to the combined  $P$ - and  $SH$ -wave dataset (Figures 4c and 5c). At depths beyond 12 km (2008 mainshock) and 18 km (2016), an east/west-striking thrust-faulting mechanism appears to yield a better fit to the observed waveforms than a north/south-striking normal-faulting mechanism (red points, Figures 4a and 5a). This thrust faulting mechanism is an artefact of the ability to produce a reduced misfit by fitting the higher amplitude part of the waveform at a subset of stations, whilst minimising the amplitude at others. Although this solution may yield a marginally better overall waveform misfit than a deep normal-faulting mechanism, it fails to fit any identifiable first motion polarities, and cannot produce an acceptable fit to the complete set of waveforms compared to a normal-faulting earthquake at shallow depths.

Whilst an increased depth can be partially offset by reducing the source duration for an individual phase, the variation in depth-phase delays at different wavespeeds (and subsequent impact on phase overlap) results in a

311 different amplitude dependence for the two phases. This trade-off is shown  
 312 in Figures 4b and 5b, which show that although the best-fit model is often  
 313 able to fit the amplitude of  $P$ -wave train at moderate depths ( $\sim 7$  km bsf), it  
 314 then significantly under-predicts the amplitude of the observed  $S$ -waveform.  
 315 This shortcoming can be partly overcome by adjusting the elastic parameters  
 316 used in the inversion, but this results in unrealistic phase separation.  
 317 Realistic variations in wavespeeds and near-source density produce only 1–2  
 318 km variation in global minimum-misfit depth. We therefore conclude that  
 319 only a shallow source depth is able to fit the amplitudes of both phases  
 320 simultaneously.

321 Absolute minimum misfit centroids for all three earthquakes occur at 2–  
 322 3 km bsf, indicating that rupture likely extended from near the seafloor to  
 323 depths of  $\sim 4$ –6 km bsf, assuming that earthquakes of this magnitude likely  
 324 rupture up to (or close to) the seafloor.

325 Best-fit focal mechanisms for all three earthquakes show north-south  
 326 striking normal faulting (consistent with routine catalogue results for low-  
 327 frequency moment tensors), with slip vectors parallel to the regional spreading  
 328 direction ( $\sim 110^\circ$ ). Source dip resolution is hampered by the lack of  
 329 along-strike  $SH$ -wave data. The best-fit mechanism is achieved, however,  
 330 with an east-dipping planar dip of  $45^\circ$  for the 2016 event and a similar  
 331 value of  $52^\circ$  for the 2008 mainshock (Figure 2b). The large uncertainty in  
 332 dip may also reflect the depth-variable dip of the curved detachment fault  
 333 surface (Figures 2b and Figure 3b). The best-fit point-source solution would  
 334 therefore represent a moment-weighted average of the fault failure surface,  
 335 and values of  $\sim 45$ – $50^\circ$  would hence be consistent with peak slip at this value  
 336 in the centre of the rupture patch. Failure would be expected over a range of  
 337 dip angles either side of this central value, consistent with failure extending  
 338 from the downdip limit of  $\sim 60$ – $65^\circ$  to the updip limit of  $\sim 30$ – $35^\circ$ .

339 The point-source approach used here assumes that the causative fault is  
 340 planar. However, if the source fault is indeed the detachment, then the rupture  
 341 patch is instead likely to be curved, hence this assumption represents  
 342 a simplification. However, synthetic waveform tests indicate that moderate  
 343 down-dip curvature makes little difference to the far-field teleseismic wave-

forms when compared to a planar-fault model (Braunmiller and Nábělek, 1996). Detection of fault curvature requires both a larger-magnitude earthquake ( $> M_w$  6) and a larger rupture dimension/rupture depth range than those near 13°20'N, to allow the resolution of discrete source orientations within the overall waveform, and also excellent along-strike *SH*-wave coverage. For earthquakes at the Mid-Atlantic Ridge where along-strike coverage is sparse, data are limited to ocean islands, the Atlantic coast of Brazil, and Iceland. While we cannot obtain evidence of down-dip curvature from the waveform data, undetectable curvature of the source fault cannot be ruled out.

Waveform inversion also yields an estimate of the shape and, of particular interest here, the duration of the source-time function. The estimated duration trades off significantly with depth (see Figures 4 and 5). However, for both the 2016 event and the 2008 mainshock, the estimated duration for the best-fit model is under 4 s, with the vast majority of the moment release taking place during a 2 s window. As increasing the source depth only serves to shorten the estimated source duration, these estimates represent maximum durations for these events. Rupture propagation speeds for dip-slip earthquakes rarely exceed the local shear-wave speed. Assuming an upper limit on the rupture velocity of 3 km s<sup>-1</sup>, the maximum dimension of the main slip patch is unlikely to exceed 6 km in any direction. The short rupture duration prevents any robust assessment of the rupture direction based on waveform directivity, and hence leaves the orientation of this maximum dimension undetermined.

## 5 Large earthquakes and the 13°20'N OCC

Slip vectors for the 2008 mainshock and 2016 earthquake (shown on Figure 1b) match to within 5° with the slip azimuth of the exposed fault surface of the OCC, inferred from the trend of surface corrugations (MacLeod et al., 2009; Escartín et al., 2017). A source mechanism and depth matching those derived from microearthquakes cannot adequately match the observed teleseismic waveforms (Figure 4b, 5b), indicating conclusively that the mi-



375 croseismicity and teleseismic earthquakes are not co-located (Parnell-Turner  
 376 et al., 2017). We conclude that the depth and source mechanism for these  
 377 earthquakes is consistent with the failure of the upper crustal section of  
 378 the detachment fault between the seafloor and the top of the observed mi-  
 379 croseismicity (7 km bsf), at moderate dip angles intermediate between the  
 380 steeply-dipping microseismicity ( $\sim 72^\circ$ ) and the observed dip of the surface  
 381 of the exposed fault ( $14\text{--}18^\circ$ ).

382 At the TAG detachment, shallow seismicity in the footwall ( $< 5$  km bsf)  
 383 has been interpreted as antithetic normal faulting (deMartin et al., 2007).  
 384 At  $13^\circ 20' \text{N}$ , no such faults are evident in microbathymetry of the exposed  
 385 fault surface (Figure 1b), nor in the microearthquake catalogue (Parnell-  
 386 Turner et al., 2017). The distribution of compressional seismicity within the  
 387 footwall indicates that any bending-related extension in the upper portion  
 388 of the footwall is probably limited to depths  $< 2$  km below the detachment  
 389 surface, consistent with the bending of a plate with elastic-plastic rheology  
 390 (Parnell-Turner et al., 2017). If the  $M_w$  5.7 event was caused by a bending-  
 391 related extensional fault within the top 2 km of the footwall block, then either  
 392 the fault must be very long in the along-strike direction, or stress drop must  
 393 be very high, in order to generate the necessary seismic moment. Given that  
 394 slip on such faults must gradually decrease to zero as the fault approaches  
 395 the depth of the neutral surface (2 km), the slip gradient required between  
 396 2 km and the surface would therefore be extremely high, and we deem this  
 397 explanation to be improbable.

398 Similar arguments apply to the hypothesis that these larger earthquakes  
 399 result from seismicity within rider blocks that could exist to the east of the  
 400 breakaway above the footwall. Multibeam bathymetric data show that any  
 401 rider blocks are restricted to the western part of the  $13^\circ 20' \text{N}$  OCC near the  
 402 breakaway (Escartín et al., 2017), and are not on the multiple-km length scale  
 403 that would be required for fault-surfaces to host  $M_w$  5.7 earthquakes without  
 404 extremely high stress drops. These rider blocks are presumably composed of  
 405 less coherent hanging wall material which has been subjected to extensive  
 406 mass wasting, and hence are unlikely to produce major earthquakes.

407 Two sub-parallel NNE-SSW trending faults, 3 km apart, can be identi-

408 fied in bathymetric data north of the 13°20'N OCC, near 13°25'N, 44°55'W  
 409 (Figure 1). These faults, which are ~10 km in length and appear to extend  
 410 from the western end of the OCC at 13°20'N to the probably inactive OCC  
 411 at 13°30'N, could potentially generate earthquakes with a rupture dimension  
 412 on order ~5 km. The dip of the exposed scarps is 40-50°, which is com-  
 413 patible with the nodal plane dips for the larger earthquakes, assuming these  
 414 faults are planar. Deep-tow sidescan sonar data show that these scarps have  
 415 low-amplitude backscatter, suggesting that they are not smooth exposures  
 416 of pristine footwall, and instead are covered in mass-wasted material or sedi-  
 417 ment (MacLeod et al., 2009). This overlying talus would have decreased the  
 418 dip angle from the true value of the fault at depth, hence these faults may  
 419 be steeper at depth than they appear on the seabed. These two small faults  
 420 were within the 2014 OBS network, which failed to detect any clustered mi-  
 421 croseismicity to indicate these faults are active. Whilst the same is true of the  
 422 shallow portion of the detachment fault, we would expect to see some degree  
 423 of microearthquake activity on the areas of the fault surrounding any patch  
 424 that ruptured in 2008 if one of these faults had hosted a larger earthquake.

425 The only other major tectonic feature within the axial valley evident in  
 426 bathymetric data is the eastern rift border fault (Figure 1a). Placing both  
 427 the 2016 event and the 2008 mainshock on this feature would require an  
 428 eastward shift of > 10 km from their globally constrained best-fitting loca-  
 429 tions. This magnitude of shift is at the limit of both the quantitative cata-  
 430 logue location uncertainty for these earthquakes [NEIC], and typical error in  
 431 global earthquake location (Lohman and Simons, 2005; Weston et al., 2012).  
 432 Whilst we cannot completely rule out this scenario, there is no evidence for  
 433 systematic westward-bias in the catalogue locations along this section of the  
 434 Mid-Atlantic Ridge to justify a common shift in both earthquake locations.

## 435 **6 Shallow detachment fault seismogenesis**

436 These results lead us to suggest that the 2008 mainshock and 2016 earthquake  
 437 most likely occurred on adjoining sections of the detachment fault at 13°20'N.  
 438 The centroid depth and overall mechanism suggest that they ruptured a

substantial area of the shallow part of the fault, extending from the near-surface emergence of the fault, down to the presumed limit of the established and contiguous fault plane, constrained by microearthquakes where the fault roots near the brittle-ductile transition.

Using the available constraints on the geometry of the detachment fault, and assuming that the 2016 earthquake and 2008 mainshock did indeed occur on the detachment surface, we can estimate the minimum stress drop for the 2008 mainshock and 2016 earthquake. The maximum area of the detachment fault that can have failed in these two earthquakes is assumed to extend from the seafloor to the upper portion of the detachment-related microseismicity in the down dip direction (0–7 km), and the spreading axis-parallel length over which microearthquakes are observed ( $\sim 15$  km). Over the downdip extent of the fault, we assume uniform curvature from  $30^\circ$  to  $70^\circ$ . We increase the estimated fault area by 5% to account for the rugosity of the fault plane, based on the three-dimensional surface area calculated for a  $2 \times 2$  km patch of the exposed fault plane using 2m-resolution microbathymetry (Escartín et al., 2017). Hence our estimated total fault area is  $1.3 \times 10^8$  m<sup>2</sup>.

Since the total along-axis extent of the detachment fault exceeds the sum of our estimated maximum rupture dimensions for the 2008 mainshock and the 2016 earthquake, we assume that each earthquake ruptured approximately half of the total fault surface available on the  $13^\circ 20' \text{N}$  detachment (based on their similar magnitudes). We then estimate a minimum stress drop,  $\Delta\sigma$ , for each earthquake by assuming  $\Delta\sigma = cM_0/(A^{(3/2)})$ , where  $A$  is the fault area,  $M_0$  is the moment, and  $c$  is a geometrical constant, approximately equal to 1. We therefore determine that  $\Delta\sigma \geq 0.68$  MPa for the 2008 mainshock, and  $\Delta\sigma \geq 0.88$  MPa for the 2016 event. These stress drops represent upper bounds, since decreasing the rupture area would increase the stress drop in each earthquake. Nonetheless, these values are consistent with stress drops observed in earthquakes in range of a tectonic regimes (Allmann and Shearer, 2009), and suggest that the detachment fault is capable of sustaining significant shear stresses throughout the upper crust, down to 6 km bsf. Hence this detachment fault appears to be rheologically comparable to globally observed normal-fault systems in non-detachment settings.

472 It is useful to compare the results presented here with the well-studied  
 473 system of detachment faults at the western end of the Woodlark Basin, south-  
 474 eastern Papua New Guinea, which is thought to mark the transition from  
 475 continental extension to oceanic spreading (Little et al., 2007; Wallace et al.,  
 476 2014). This region contains several active detachment faults and associ-  
 477 ated core complexes, including the type-examples of the sub-aerial Dayman  
 478 Dome, and the sub-marine Moresby Seamount detachment (Spencer, 2010;  
 479 Speckbacher et al., 2011). Crucially, these faults have been shown to host  
 480 large-magnitude ( $>M\ 6.0$ ), shallowly-dipping normal-faulting earthquakes at  
 481 shallow depth (Abers, 1991; Abers et al., 1997). Although these detachments  
 482 are exhuming high-pressure metamorphic rocks in their footwalls, rather than  
 483 newly-formed igneous oceanic crust, the detachment-faulting process has  
 484 been suggested to be common to both regimes (e.g. Abers et al., 1997; Little  
 485 et al., 2007). Despite the presence of large-scale seismicity, recent geodetic  
 486 work has suggested that much of the slip on these faults is accommodated  
 487 aseismically through stable sliding on unlocked faults (Wallace et al., 2014),  
 488 although we note that the proposed coupling models did require locked faults  
 489 at shallow depth. In common with observations from oceanic detachment sys-  
 490 tems, these faults are characterised by coincident mylonitization, alteration  
 491 to phyllosilicate minerals, and widespread precipitation of hydrothermal cal-  
 492 cite and quartz, based on in samples dredged from the Moresby Seamount  
 493 detachment fault (Speckbacher et al., 2011).

494 Lower-crustal gabbros and mantle peridotites exposed on oceanic detach-  
 495 ment footwalls are commonly altered to sheet silicates such as talc and chlo-  
 496 rite due to pervasive hydrous circulation (e.g. Dick, 1989; Blackman et al.,  
 497 2002; Escartín et al., 2003; Karson et al., 2006; Blackman et al., 2014). The  
 498 presence of these low-friction minerals suggests that within the shallow crust,  
 499 slip may occur through aseismic creep along a rheologically weak fault sur-  
 500 face, implying that the shallow portion of a detachment fault would be unable  
 501 to support the stresses necessary to produce earthquakes (Escartín et al.,  
 502 1997; deMartin et al., 2007). In contrast, in-situ sampling of the corrugated  
 503 dome at  $13^{\circ}20'N$  shows that, although heavily-altered ultrabasic rocks and  
 504 talc are present, the exposed fault surface predominantly consists of quartz-

505 cemented cataclastic metadiabase (Bonnemains et al., 2017). These rocks  
506 are probably sourced from the hanging wall and later incorporated into the  
507 fault zone within the uppermost few kilometres of the crust (Bonnemains  
508 et al., 2017). Whilst this zone is unlikely to account for the full rupture  
509 area of the larger earthquakes studied here, the migration of rupture into a  
510 hanging wall comprised of quartz-cemented breccia suggests that the fault  
511 surface must be at least as strong as this material. Hence the fault rheology,  
512 even at shallow depths, is not dominated by minerals with low coefficients of  
513 static friction—consistent with the presence of shear stresses large enough to  
514 produce large earthquakes.

515 The rheological behaviour of the materials most likely to dominate the  
516 fault zone (gabbroic rocks and hydrous alteration products) is highly temper-  
517 ature dependent (e.g. Chernak and Hirth, 2010; Moore and Lockner, 2011).  
518 A combination of variable fault rock composition and rheology, the complex  
519 thermal structure at the spreading axis, and the unquantified influence of  
520 variable pore fluid pressure, fault zone rheology remains highly uncertain.  
521 The ability to generate large earthquakes within the uppermost few kilo-  
522 metres of the fault, however, requires that the overall fault rheology in this  
523 region be velocity-weakening. It remains unclear why the presence of weak  
524 hydrous minerals does not appear to have inhibited seismogenic failure, or  
525 had a major weakening effect on the fault itself, at least on the timescale of  
526 the earthquake cycle.

527 At 13°20'N, the apparent occurrence of large-magnitude earthquakes on  
528 the shallow part of the detachment fault contrasts with the microseismicity  
529 that characterises the deeper, steeper-dipping sections (Figure 7), and raises  
530 questions about what controls the transition in seismogenic character over  
531 seemingly short length scales at depth. One important factor is likely to be  
532 the thermal profile within the fault zone. However, the thermal structure  
533 of oceanic detachment fault systems is difficult to ascertain with any accu-  
534 racy, as a result of the complex interplay between magmatic processes, the  
535 formation of new oceanic lithosphere, and widespread hydrothermal perco-  
536 lation, controlled by the local permeability structure. The thermal structure  
537 is intrinsically linked to the rheological evolution of the fault zone material,

538 which controls on the capacity of the fault zone to sustain stresses. The evo-  
 539 lution of the fault itself as the footwall is exhumed may also play a role, since  
 540 the active fault is thought to emerge from a ductile mylonitic shear zone at  
 541 depth (Hansen et al., 2013). The fault may develop as strain is localized on  
 542 many small brittle cracks at intermediate depths, forming as a finite-thickness  
 543 layer with an anastomosing fabric while generating microearthquakes (Kar-  
 544 son et al., 2006; Bonnemains et al., 2017), before coalescing into a single  
 545 coherent fault zone nearer to the surface. The transition between failure in  
 546 many microearthquakes to failure in large earthquakes at  $\sim 5$  km bsf may  
 547 therefore represent the point at which microcracks coalesce, thus establish-  
 548 ing a continuous fault plane, and allowing rupture to propagate continuously  
 549 over large areas.

550 Earlier studies of large earthquakes at slow-spreading ridges have shown  
 551 that teleseismically-detected earthquakes commonly occur with centroid depths  
 552 of  $< 4$  km bsf and at dip angles of  $45^\circ$ , within the uppermost oceanic litho-  
 553 sphere (Huang et al., 1986; Jemsek et al., 1986; Huang and Solomon, 1987).  
 554 Supra-source water depths from  $P$ -wave multiples indicate that majority of  
 555 these larger earthquakes occurred beneath the axial valley, potentially con-  
 556 sistent with their occurrence on the down-dip section of detachment faults.  
 557 However, lacking the bathymetric and microearthquake data to identify ac-  
 558 tive detachment faulting, these poorly-understood events had been assumed  
 559 to represent slip on rift-bounding border faults. The similarity in dip and  
 560 depth to the teleseismically-detected earthquakes at  $13^\circ 20'N$  suggests that  
 561 this may not be the case, and instead, slip on the shallow portion of de-  
 562 tachment faults may be responsible for many more large earthquakes than  
 563 previously recognised. This inference is consistent with increased rates of  
 564 seismic moment release at detachment-dominated spreading segments, and  
 565 with increased estimated for the thickness of the coupled seismogenic layer  
 566 (Escartín et al., 2008; Olive and Escartín, 2016).

## 567 **7 Conclusions**

568 We find that large earthquakes at 13°20'N on the MAR are best explained  
569 by rupture on the shallow, gently-dipping portion of a detachment fault. At  
570 depths of  $\sim 10$  km bsf, where the fault is presumed to initiate, a network  
571 of local fractures give rise to small magnitude microearthquakes which are  
572 undetected by the global teleseismic network. At shallower depths, these  
573 smaller rupture patches coalesce into a coherent fault plane, strong enough to  
574 produce large earthquakes which rupture substantial portions of the shallow  
575 fault surface. Despite the presence of weak minerals and a transition to  
576 dip-angles usually thought to be too low to support seismogenic failure, our  
577 results show that oceanic detachment faults may be strong, and generate  
578 earthquakes in the uppermost  $\sim 7$  km of the lithosphere, in common with  
579 those found on the continents.

## 580 **Acknowledgements**

581 TJC thanks the Royal Commission for the Exhibition of 1851 for financial  
582 support through a Research Fellowship; RPT was supported by NSF grant  
583 OCE-1458084. Several figures were produced using the Generic Mapping  
584 Tools software package. Seismic data were retrieved from the IRIS Data  
585 Management Center. We thank Rob Sohn and Javier Escartín for their  
586 comments on a draft manuscript, and we thank the editor and two anonymous  
587 reviewers for their comments.

## References

- G.A. Abers. Possible seismogenic shallow-dipping normal faults in the Woodlark-D'Entrecasteaux extensional province, Papua New Guinea. *Geology*, 19, 1991.
- G.A. Abers, C.Z. Mutter, and J. Fang. Shallow dips of normal faults during rapid extension: Earthquakes in the Woodlark-D'Entrecasteaux rift system, Papua New Guinea. *Journal of Geophysical Research*, 102:15301–15317, 1997.
- B.P. Allmann and P.M. Shearer. Global variations of stress drop for moderate to large earthquakes. *Journal of Geophysical Research*, 114, 2009. doi: 10.1020/2008JB005821.
- D K Blackman, J P Canales, and A. J. Harding. Geophysical signatures of oceanic core complexes. *Geophys. J. Int.*, 178(2):593–613, 2009. doi: 10.1111/j.1365-246X.2009.04184.x.
- D.K. Blackman, J.A. Karson, D.S. Shelly, J.R. Cann, G.L. Früh-Green, J. S. Gee, S.D. Hurst, B.E. John, J. Morgan, S.L. Nooner, D.K. Ross, T.J. Schroeder, and E.A. Williams. Geology of the Atlantis Massif (Mid-Atlantic Ridge, 30°N): Implications for the evolution of an ultramafic oceanic core complex. *Marine Geophysical Researches*, 23:443–469, 2002.
- D.K. Blackman, A. Slagle, G. Guerin, and A. Harding. Geophysical signatures of past and present hydration within a young oceanic core complex. *Geophysical Research Letters*, 41:1179–1186, 2014. doi: 10.1002/2013GL058111.
- B. Bonnemains, J. Escartín, C. Mével, M. Andreani, and A. Verlaquet. Pervasive silicification and hangingwall overplating along the 13°20'N oceanic detachment fault (Mid-Atlantic Ridge). *Geochemistry, Geophysics, Geosystems*, 18:2028–2053, 2017. doi: 10.1002/2017GC006846.



615 J. Braunmiller and J. Nábêlek. Geometry of continental normal faults: Seis-  
616 mological constraints. *Journal of Geophysical Research*, 101:3045–3052,  
617 1996.

618 J.R. Cann, D. K. Blackman, D.K. Smith, E. McAllister, B. Janssen, S. Mello,  
619 S. Avgerinos, and E. Pascoe. Corrugated slip surfaces formed at ridge-  
620 transform intersections on the Mid-Atlantic Ridge. *Nature*, 385:329–332,  
621 1997.

622 L.J. Chernak and G. Hirth. Deformation of antigorite serpentinite at high  
623 temperature and pressure. *Earth and Planetary Science Letters*, 296:23–33,  
624 2010.

625 T. J. Craig, A. Copley, and J. Jackson. A reassessment of outer-rise seismicity  
626 and its implications for the mechanics of oceanic lithosphere. *Geophysical*  
627 *Journal International*, 197:63–89, 2014. doi: 10.1093/gji/ggu013.

628 Brian J deMartin, R. A. Sohn, J P Canales, and Susan E Humphris. Kinemat-  
629 ics and geometry of active detachment faulting beneath the Trans-Atlantic  
630 Geotraverse (TAG) hydrothermal field on the Mid-Atlantic Ridge. *Geology*,  
631 35:711–714, 2007. doi: 10.1130/G23718A.1.

632 H J B Dick, M A Tivey, and B E Tucholke. Plutonic foundation of a slow-  
633 spreading ridge segment: Oceanic core complex at Kane Megamullion,  
634 23°30’N, 45°20’W. *Geochem. Geophys. Geosyst.*, 9(5):Q05014, 2008. doi:  
635 10.1029/2007GC001645.

636 H.J.B. Dick. Abyssal peridotites, very slow spreading ridges and ocean ridge  
637 magmatism. *Geological Society Special Publications*, 42:71–105, 1989.

638 J. Escartin and J P Canales. Chapman Conference on Detachments in  
639 Oceanic Lithosphere: Deformation, Magmatism, Fluid Flow and Ecosys-  
640 tems. *Eos Trans. AGU*, 92:31, 2011. doi: 10.1029/2011EO040003.

641 J. Escartín, G. Hirth, and B Evans. Effects of serpentinization on the litho-  
642 spheric strength and the style of normal faulting at slow-spreading ridges.  
643 *Earth Planet. Sci. Lett.*, 151(3-4):181–189, 1997.

- 644 J. Escartín, C. Mével, C.J. MacLeod, and A.M. McCaig. Constraints on  
645 deformation conditions and the origin of oceanic detachments: The Mid  
646 Atlantic ridge core complex at 15°45'N. *Geochemistry, Geophysics, Geosys-*  
647 *tems*, 4, 2003. doi: 10.1029/2002GC000472.
- 648 J. Escartín, D.K. Smith, J. Cann, C.H. Langmuir, and S. Escrig. Central  
649 role of detachment faults in accretion of slow-spreading oceanic lithosphere.  
650 *Nature*, 455, 2008.
- 651 J. Escartín, C. Mével, S. Petersen, D. Bonnemains, M. Cannat, M. Andreani,  
652 N. Augustin, A. Bezos, V. Chavagnac, Y. Choi, M. Godard, K. Haaga,  
653 C. Hamelin, B. Ildefonse, J. Jamieson, B. John, T. Leleu, C.J. MacLeod,  
654 M. Massot-Campos, P. Nomikou, J.A. Olive, M. Paquet, C. Rommevaux,  
655 M. Rothenbeck, A. Steinfuhrer, M. Tominaga, L. Triebe, R. Campos,  
656 N. Gracias, and R. Garcia. Tectonic structure, evolution and the nature  
657 of oceanic core complexes and their detachment fault zones (13°20'N and  
658 13°30'N, Mid Atlantic Ridge). *Geochemistry, Geophysics, Geosystems*, 18,  
659 2017. doi: 10.1002/2016GC006775.
- 660 W.I. Futterman. Dispersive body waves. *Journal of Geophysical Research*,  
661 67:5279–5291, 1962.
- 662 I. Grevemeyer, T.J. Reston, and S. Moeller. Microseismicity of the Mid-  
663 Atlantic Ridge at 7°–8°15'S and at the Logatchev Massif oceanic core  
664 complex at 14°40'N–14°50'N. *Geochemistry, Geophysics, Geosystems*, 14:  
665 3532–3554, 2013. doi: 10.1002/ggge.20197.
- 666 L.N. Hansen, M.J. Cheadle, B.E. John, S.M. Swapp, H.J.B. Dick, B.E.  
667 Tucholke, and M.A. Tivey. Mylonitic deformation at the Kane oceanic  
668 core complex: Implications for the rheological behaviour of oceanic de-  
669 tachment faults. *Geochemistry, Geophysics, Geosystem*, 14, 2013. doi:  
670 10.1002/ggge20184.
- 671 P. Y. Huang and S. C. Solomon. Centroid Depths and Mechanisms of Mid-  
672 Ocean Ridge Earthquakes in the Indian, Gulf of Aden, and Red Sea. *Jour-*  
673 *nal of Geophysical Research*, 92:1361–1382, 1987.

- 674 P. Y. Huang, S.C. Solomon, E. A. Bergman, and J.L. Nabelek. Focal Depths  
675 and Mechanisms of Mid-Atlantic Ridge Earthquakes from Body Waveform  
676 Inversion. *Journal of Geophysical Research*, 91:579–598, 1986.
- 677 International Seismological Centre. *On-line bulletin*. Int. Seis. Cent.,  
678 Thatcham, United Kingdom, 2014. <http://www.isc.ac.uk>.
- 679 J.P. Jemsek, E.A. Bergman, J.L. Nabelek, and S.C. Solomon. Focal Depths  
680 and Mechanisms of Large Earthquakes on the Arctic Mid-Ocean Ridge  
681 System. *Journal of Geophysical Research*, 91:13993–14005, 1986.
- 682 J.A. Karson, G.L. Fruh-Green, D.S. Kelley, E.A. Williams, D.R. Yoerger, and  
683 M. Jakuba. Detachment shear zone of the Atlantis Massif core complex,  
684 Mid-Atlantic Ridge, 30°N. *Geochemistry, Geophysics, Geosystems*, 7, 2006.  
685 doi: 10.1029/2005GC001109.
- 686 L.S.L. Kong, S.C. Solomon, and G.M. Purdy. Microearthquake Character-  
687 istics of a Mid-Ocean Ridge Along-Axis High. *Journal of Geophysical*  
688 *Research*, 97:1659–1685, 1992.
- 689 T.A. Little, S.L. Baldwin, P.G. Fitzgerald, and B. Montelone. Continental  
690 rifting and metamorphic core complex formation ahead of the Woodlark  
691 spreading ridge, D’Entrecasteaux Islands, Papua New Guinea. *Tectonics*,  
692 26, 2007. doi: 10.1029/2005TC001911.
- 693 R.B. Lohman and M. Simons. Locations of selected small earthquakes in the  
694 Zagros mountains. *Geochemistry, Geophysics, Geosystems*, 6, 2005. doi:  
695 10.1029/2004GC000849.
- 696 C.J. MacLeod, J. Escartín, D. Banerji, G.J. Banks, M. Gleeson, D.H.B. Irv-  
697 ing, R. M. Lilly, A.M. McCaig, Y. Niu, S. Allerton, and D.K. Smith. Di-  
698 rect geological evidence for oceanic detachment faulting: The Mid-Atlantic  
699 Ridge, 15°45’N. *Geology*, 30:879–88, 2002.
- 700 C.J. MacLeod, R.C. Searle, B.J. Murton, J.F. Casey, C. Mallows, S.C.  
701 Unsworth, K.L. Achenback, and M. Harris. Life cycle of oceanic core

702 complexes. *Earth and Planetary Science Letters*, 287:333–344, 2009. doi:  
703 10.1016/j.epsl.2009.08.016.

704 C. Mallows and R.C. Searle. A geophysical study of oceanic core complexes  
705 and surrounding terrain, Mid-Atlantic Ridge 13°-14°N. *Geochemistry,*  
706 *Geophysics, Geosystems*, 13, 2012. doi: 10.1020/2012GC004075.

707 D. E. Moore and D. A. Lockner. Frictional strengths of talc-serpentine and  
708 talc-quartz mixtures. *Journal of Geophysical Research*, 116, 2011. doi:  
709 10.1029/2010JB007881.

710 A. Morris, J S Gee, N. Pressling, B. E. John, C J MacLeod, C. B. Grimes,  
711 and R C Searle. Footwall rotation in an oceanic core complex quantified  
712 using reoriented Integrated Ocean Drilling Program core samples. *Earth*  
713 *Planet. Sci. Lett.*, 287(1-2):217–228, 2009. doi: 10.1016/j.epsl.2009.08.007.

714 J.-A. Olive and J. Escartín. Dependence of seismic coupling on normal fault  
715 style along the Northern Mid-Atlantic Ridge. *Geochemistry, Geophysics,*  
716 *Geosystems*, 17:4128–4152, 2016. doi: 10.1002/2016GC006460.

717 R Parnell-Turner, R. A. Sohn, C. Peirce, T J Reston, C J Macleod, R C  
718 Searle, and N. M. Simão. Oceanic Detachment Faults Generate Compression  
719 in Extension. *Geology*, 2017. doi: 10.1130/G39232.1.

720 N. Simão, C. Peirce, Matthew Falder, T J Reston, C J Macleod, and R C  
721 Searle. Velocity structure of the crust at 13N on the Mid-Atlantic Ridge:  
722 implications for crustal accretion and oceanic core complex formation. *Abstract T33A-2997 presented at 2016 Fall Meeting, AGU, San Francisco,*  
723 *Calif. 12-16 Dec*, 2016.

725 D.K. Smith, J.R. Cann, and J. Escartín. Widespread active detachment  
726 faulting and core complex formation near 13°N on the Mid-Atlantic Ridge.  
727 *Nature*, 442:440–443, 2006.

728 S.C. Solomon and P.Y. Huang. Centroid depths and mechanisms of mid-  
729 ocean ridge earthquakes in the Indian Ocean, Gulf of Aden, and Red Sea.  
730 *Journal of Geophysical Research*, 92:1361–1382, 1987.

- 731 R. Speckbacher, J.H. Behrmann, T.J. Nagel, M. Stipp, and C.W. Devey.  
732 Splitting a continent: Insight from submarine high-resolution mapping of  
733 the Moresby Seamount detachment, offshore Papua New Guinea. *Geology*,  
734 39:651–654, 2011. doi: 10.1130/G31931.1.
- 735 J.E. Spencer. Structural analysis of three extensional detachment faults with  
736 data from the 2000 Space-Shuttle Radar Topography Mission. *GSA Today*,  
737 20:4–10, 2010.
- 738 L.R. Sykes. Mechanism of earthquakes and nature of faulting on the mid-  
739 ocean ridges. *Journal of Geophysical Research*, 72:2131–2153, 1967.
- 740 F. J. Tilmann, T. J. Craig, I. Grevemeyer, B. Suwargadi, H. Kopp, and  
741 E. Flueh. The updip seismic/aseismic transition of the Sumatra megath-  
742 rust illuminated by aftershocks of the 2004 Aceh-Andaman and 2005 Nias  
743 events. *Geophysical Journal International*, 181:1261–1274, 2010. doi:  
744 10.1111/j.1365-246X.2010.04597.x.
- 745 D.R. Toomey, S.C. Solomon, G.M. Purdy, and M.H.H. Murray. Mi-  
746 croearthquakes beneath the median valley of the Mid-Atlantic Ridge near  
747 23°N: Hypocenters and focal mechanisms. *Journal of Geophysical Re-  
748 search*, 90:5443–5458, 1985.
- 749 B.E. Tucholke, J. Lin, and M.C.C. Kleinrock. Megamullions and mul-  
750 lion structure defining oceanic metamorphic core complexes on the Mid-  
751 Atlantic Ridge. *Journal of Geophysical Research*, 103:9857–9866, 1998.
- 752 L.M. Wallace, S. Ellis, P. Tregoning, N. Palmer, R. Rosa, R. Stanaway,  
753 J. Oa, E. Nidkombu, and J. Kwazi. Continental breakup and UHP rock  
754 exhumation in action: GPS results from the Woodlark Rift, Papua New  
755 Guinea. *Geochemistry, Geophysics, Geosystems*, 15:4267–4290, 2014. doi:  
756 10.1002/2014GC005458.
- 757 J. Weston, A. G. Ferreira, and G.J. Funning. Systematic comparisons  
758 of earthquake source models determined using InSAR and seismic data.  
759 *Tectonophysics*, 532-535:61–81, 2012. doi: 10.1016/j.tecto.2012.02.001.

- 760 C.J. Wolfe, G.M. Purdy, D.R. Toomet, and S.C. Solomon. Microearthquake  
761 characteristics and crustal velocity structure at 29°N on the Mid-Atlantic  
762 Ridge: The architecture of a slow spreading segment. *Journal of Geophys-*  
763 *ical Research*, 100:24449–24472, 1995.
- 764 P. Zwick, R. McCaffrey, and G. Abers. MT5 program. *IASPEI Software*  
765 *Library*, 4, 1994.

Identifier	Date & Time	Depth (km bsl)	Moment (N m)	$M_w$	Strike (°)	Dip (°)	Rake (°)
Microseismicity	-	10–14	-	-	352	72	-105
2008 Mainshock	2008/12/07 06:23:10	6.0	$3.555 \times 10^{17}$	5.7	343	52	-104
2008 Aftershock	2008/12/08 01:51:01	5.0	$2.663 \times 10^{17}$	5.6	350	46	-093
2016	2016/10/20 00:09:26	5.1	$4.620 \times 10^{17}$	5.7	345	45	-105

Table 1: **Mechanism parameters for seismicity near 13°20’N.** Values for microseismicity are taken from Parnell-Turner et al. (2017). Values for the three larger earthquakes are based on waveform modelling (this study), shown in Figures S2–S4.

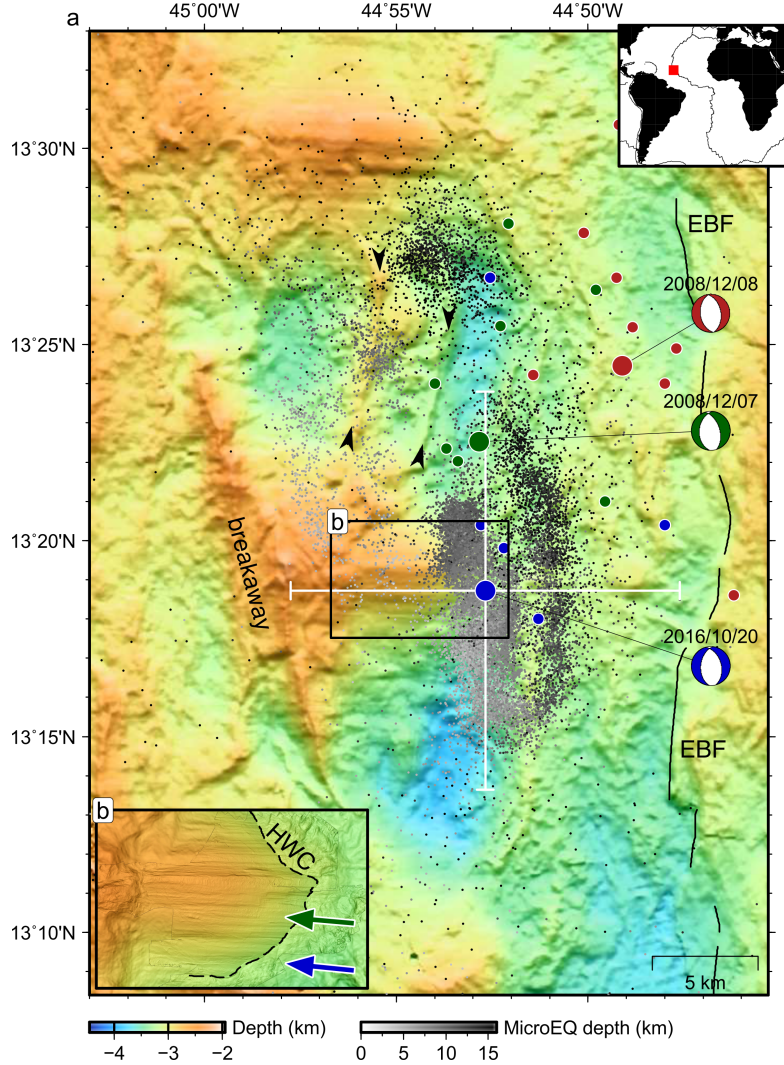


Figure 1: **Bathymetry and earthquakes.** Inset: red box shows study location. (a) Small dots are microearthquakes shaded by depth (Parnell-Turner et al., 2017); large blue circle is preferred hypocentre for  $M_w$  5.7 event on 20<sup>th</sup> October 2016 (NEIC catalogue); large green/red circles are hypocentres for  $M_w$  5.6/5.5 events on 7<sup>th</sup>/8<sup>th</sup> December 2008 events, respectively (ISC catalogue); focal mechanisms shown are best fitting solutions from this study; small coloured circles are unfavoured hypocentres from alternative catalogues (see Table S1 for details); solid black line is eastern border fault (EBF); arrow tips mark small fault scarps near OCC. (b) Detailed view of corrugated fault surface, with 2 m resolution microbathymetry (Escartín et al., 2017, French Oceanographic Cruises, <http://dx.doi.org/10.17600/13030070>), blue/green arrows indicate slip direction of 2016/2008 main shocks, respectively; dashed line is hanging wall cutoff (HWC).



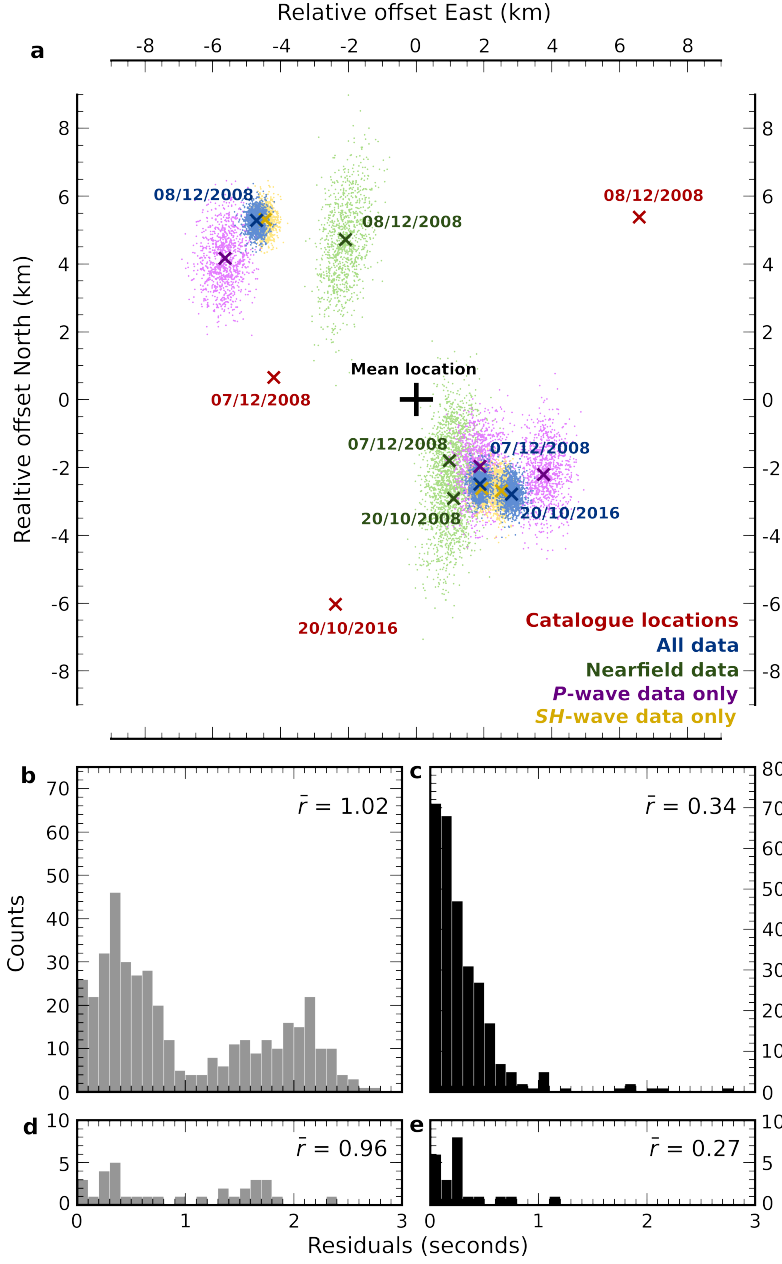


Figure 2: **Relative relocation of teleseismic earthquakes.** (a) Relative earthquake locations for the three teleseismically-observed events. Sets of locations are shown relative to their common mean, defined as plot origin, shown by large black cross. Red crosses are initial catalogue locations. Blue crosses are locations after relocation using all data. Green crosses are relocations using only data at epicentral distances  $< 30^\circ$ . Purple/yellow crosses are relocations using only *P*-wave/*SH*-wave data, respectively. Small coloured points show 1000 relocations after relative time dataset has been randomly perturbed based on a normal distribution of width defined by mean post-relocation residual. (b) Cross-correlation derived residuals prior to relocation for all data.  $\bar{r}$  indicates the mean residual. (c) Residuals after relocation using all data. (d),(e) as for (b),(c), but showing residuals for relocation using only data at epicentral angles  $< 30^\circ$ .

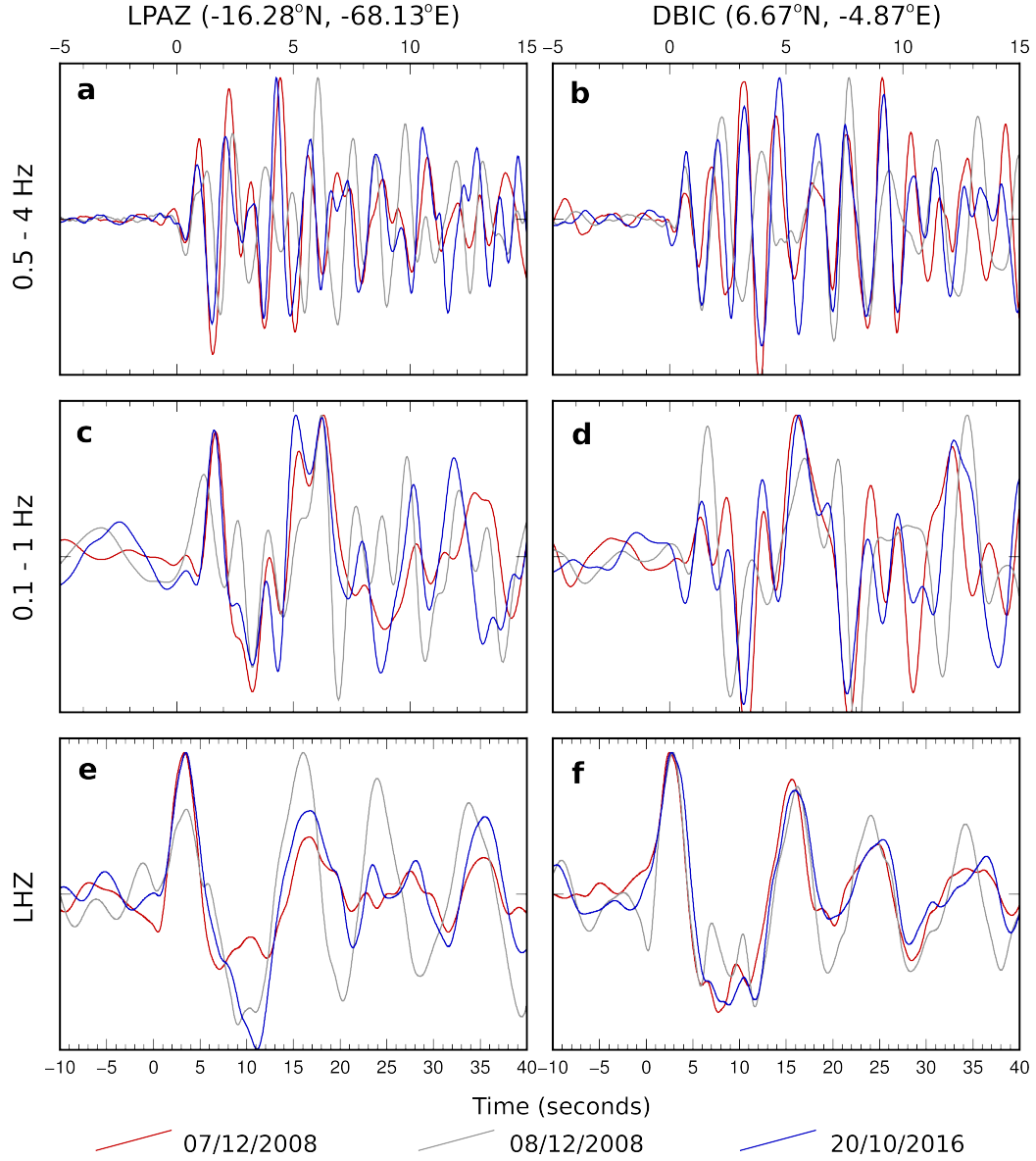


Figure 3: **Waveform comparisons at different frequency bands.** Left column shows waveforms from station LPAZ in Bolivia. Right column shows waveforms from station DBIC in Cote d'Ivoire. Waveforms aligned relative to *P*-wave arrival. (a,b) Waveforms subject to 4-pole Butterworth filter with pass band 0.5–4 Hz. (c,d) Waveforms subject to 4-pole Butterworth filter with pass band 0.1–1 Hz. (e,f) Waveforms converted to tapered frequency response of a long-period seismometer.

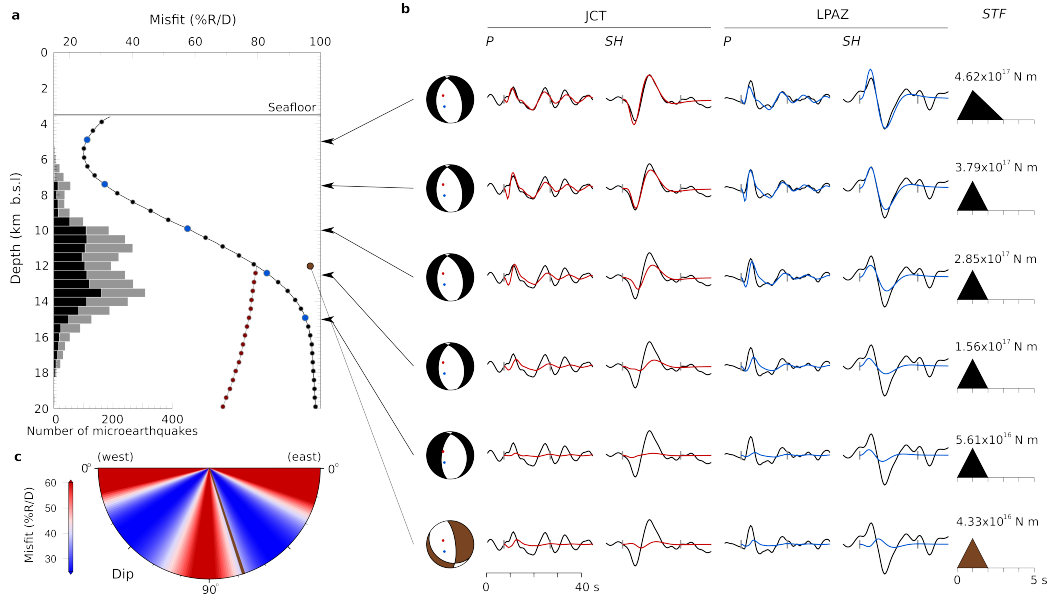


Figure 4: **Analysis of 7<sup>th</sup> December 2008 earthquake.** (a) Waveform misfit as a function of depth. Black line/points are for solutions with prior assumption of north-striking normal fault. Blue points indicate depth values used for sensitivity examples shown in b. Grey line/red points are for fully unconstrained solutions. Histograms show depth of extensional microearthquakes from Parnell-Turner et al. (2017), grey for all extensional earthquakes, black for only those adjacent to corrugated dome at 13°20'N. (b) Depth-sensitivity tests at depths of 5, 7.5, 10, 12.5, and 15 km bsl. Left column shows best-fit focal mechanism for each depth interval. Red/blue points show projection of two example stations, JCT and LPAZ, respectively. Following four columns show *P*- and *SH*-waveforms for stations JCT and LPAZ. Black traces are observed waveforms, coloured traces are synthetic waveforms for best-fit solution at each depth. Black vertical ticks indicate inversion window. Right hand column shows best-fit source-time function and moment for each depth. Bottom row shows waveforms calculated with depth and mechanism fixed to match values for microearthquake composite mechanism (Parnell-Turner et al., 2017). (c) Dip sensitivity tests. Brown bar shows dip value of composite focal mechanism for normal-faulting microseismicity at base of detachment fault (72°).

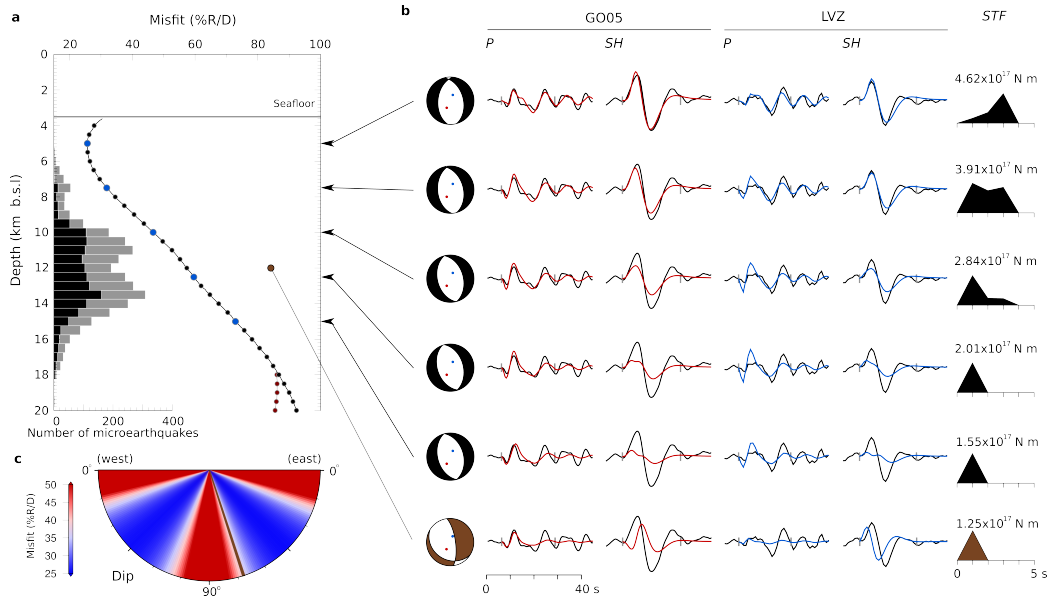


Figure 5: **Analysis of 20<sup>th</sup> October 2016 earthquake.** (a) As in Figure 4. (b) As in Figure 4, except with stations G005 and LVZ substituted for JCT and LPAZ. (c), (d) As in Figure 4.

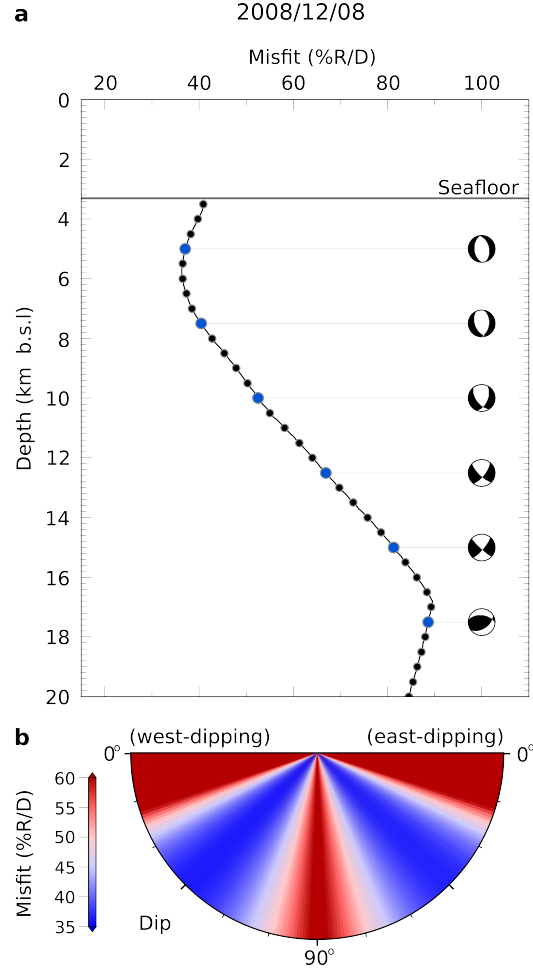


Figure 6: **Analysis of 8<sup>th</sup> December 2008 earthquake.** (a) Waveform misfit as a function of depth, calculated at 0.1 km depth intervals. At each depth, best-fit solution is calculated based on free inversion for all source parameters, except depth. Best-fit focal mechanisms shown at 2.5 km increments. (b) Dip sensitivity tests for east-most and west-most dipping planes for 8<sup>th</sup> December 2008 earthquake. At each dip-value, dip and centroid depth are fixed (at overall best-fit value for centroid depth), while all other parameters vary freely.

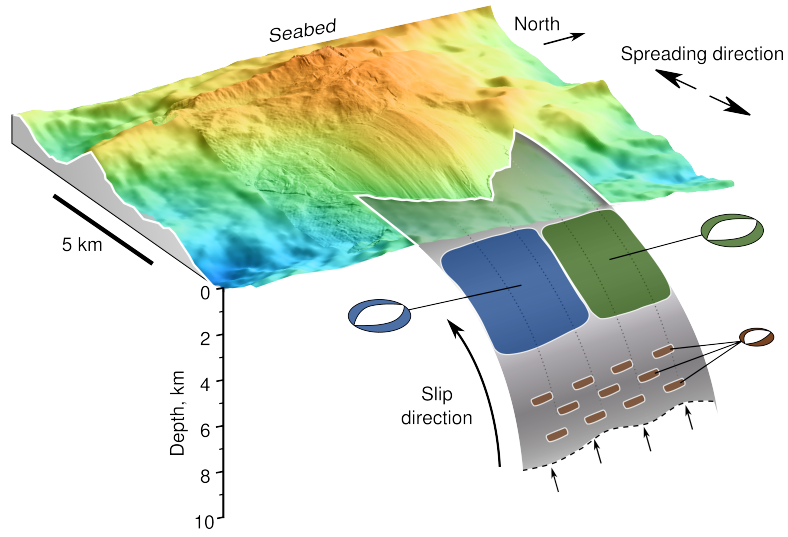


Figure 7: **Three-dimensional sketch showing bathymetry and rupture at 13°20'N detachment fault.** Grey curved area is portion of detachment fault surface; focal mechanism solutions and rupture patches for 2016 event (blue), 2008 mainshock (green) and subset of microearthquakes (brown) plotted in their expected positions on fault surface. Black arrows show spreading/slip direction. Microbathymetry from (Escartín et al., 2017, French Oceanographic Cruises, <http://dx.doi.org/10.17600/13030070>), with colour shading as in Figure 1.